

Cite this article as: Zhang Mengdi, Zhang Gaimei, Luo Chongwei, et al. Effect of Aluminum Content on Microstructure and Tribological Properties of CoCrFeNi₂-Based High-Entropy Alloys[J]. Rare Metal Materials and Engineering, 2025, 54(02): 343-353. <https://doi.org/10.12442/j.issn.1002-185X.20240625>.

ARTICLE

Effect of Aluminum Content on Microstructure and Tribological Properties of CoCrFeNi₂-Based High-Entropy Alloys

Zhang Mengdi, Zhang Gaimei, Luo Chongwei, Xu Hanqing

School of Quality and Technical Supervision, Hebei University, Baoding 071002, China

Abstract: Four machine learning algorithms were used to predict the solid solution phases of high-entropy alloys (HEAs). To improve the model accuracy, the K-fold cross validation was adopted. Results show that the K-nearest neighbor algorithm can effectively distinguish body-centered cubic (bcc) phase, face-centered cubic (fcc) phase, and mixed (fcc+bcc) phase, and the accuracy rate is approximately 93%. Thereafter, CoCrFeNi₂Al_x (x=0, 0.1, 0.3, 1.0) HEAs were prepared and characterized by X-ray diffractometer and energy disperse spectrometer. It is found that their phases are transformed from fcc phase to fcc+bcc phase, which is consistent with the prediction results of machine learning. Furthermore, the influence of Al content on the microstructure and tribological properties of CoCrFeNi₂Al_x (x=0, 0.1, 0.3, 1.0) HEAs was evaluated. Results reveal that with the increase in Al content, the nanohardness and microhardness increase by approximately 45% and 75%, respectively. The elastic limit parameter H/E_r increases from 0.0216 to 0.030, whereas the plastic deformation resistance parameter H^3/E_r^2 increases from 0.0014 to 0.0045, which demonstrates an improvement in nanohardness with the increase in Al addition amount. In addition, the wear rate decreases by 35% with the increase in Al addition amount. This research provides a new idea with energy-saving and time-reduction characteristics to prepare HEAs.

Key words: machine learning; high-entropy alloy; hardness; wear resistance

In recent years, high-entropy alloys (HEAs) have become one of the hotspot materials as a new type of metallic material. HEAs are composed of at least four principal elements with approximately equal atomic ratios^[1]. The atomic molar percentages of each element in the alloy range between 5at% and 35at%^[2-3]. HEAs have superb properties, such as high hardness, high strength, fine oxidation resistance, and good corrosion resistance^[4], therefore attracting much attention on their composition design and property enhancement.

The traditional trial-and-error experiment approach is not only time-consuming and costly but also demands stringent conditions, resulting in difficulty to conduct multiple experiments in a short period. As research progresses, computational intelligence simulation methods have been applied to design HEAs, such as first-principles calculations^[5], parameter methods^[6], and CALPHAD method^[7]. Although the conventional methods are relatively accurate in HEAs study, their high cost and multiple influencing factors involved make

the design process quite challenging.

The recent integration of artificial intelligence-driven machine learning (ML) has emerged as a potent strategy for the design of novel multicomponent alloy systems. The versatility and algorithmic generalization capabilities of ML not only expedite the design process but also promote the cost-effective procedure. Using multipurpose learning, ML algorithms can rapidly identify patterns and relationships within complex datasets, thereby streamlining the development of new alloy systems with enhanced properties. Bobbili et al^[8] predicted the phases in HEAs through ML and found the XGBoost algorithm could achieve the accuracy rate of 90%. Guo et al^[9] predicted the phases in HEAs and reported that the prediction accuracy rate was over 89% for intermetallic compounds and over 98% for solid solutions and amorphous phases. Li et al^[10] used ML and material descriptor selection by enhanced genetic algorithm to predict the hardness of HEAs in the Al-Co-Cr-Cu-Fe-Ni system. Oñate et

Received date: September 27, 2024

Foundation item: National Natural Science Foundation of China (52201177); Hebei Province Department of Education Fund (QN2024264); Natural Science Foundation of Hebei Province (E2022201010)

Corresponding author: Xu Hanqing, Ph. D., Professor, School of Quality and Technical Supervision, Hebei University, Baoding 071002, P. R. China, E-mail: xuhanqing@hbu.edu.cn

Copyright © 2025, Northwest Institute for Nonferrous Metal Research. Published by Science Press. All rights reserved.

al^[11] applied ML to 2434 experiment data for phase prediction, and the optimal evaluation model was Random Forest model with the accuracy rate of 72.8%. Although multiple researches have been conducted by ML, the application of ML in the realm of HEAs is still in its nascent stage, and several challenges may impede its effectiveness. The absence of comprehensive experiment database and the irrational selection of feature combinations can lead to significant predictive uncertainties.

HEAs are considered as effective wear-resistant materials. Jiang et al^[12] investigated the microstructure and tribological properties of the Co-Fe-Ni-V-Zr HEAs. It is concluded that with Zr addition and grain size reduction, the wear resistance is greatly increased. Yu et al^[13] found that the wear resistance of the Co-Cr-Fe-Ni-Nb HEAs was superior, compared with that of Inconel 718 alloy. Zhang et al^[14] investigated the impact of Al content on the wear resistance of Al-Cr-Ti-Mo alloy system, and concluded that increasing the Al content could enhance the wear resistance. Furthermore, based on the Archard wear equation, the wear resistance of a material is directly related to its hardness^[15]. For instance, Liu et al^[16] prepared the CoCrFeNiW_x ($x=0, 0.25, 0.50, 0.75, 1.00$) HEAs and reported that with the increase in W content, the microhardness is increased and the wear resistance is improved significantly. Xing et al^[17] found that the Al-doping could lead to the reduction in the coefficient of friction (COF) and the increase in hardness, thereby improving the wear resistance. Moreover, with higher Al content, the primary wear mechanisms were identified as abrasive wear and oxidative wear. Wu et al^[18] reported that the addition of Ti could enhance both the hardness and oxidation resistance of AlCrFeCoNi HEA, resulting in better wear performance. These studies all provide valuable insights into the tribological properties of HEAs. Despite the extensive research on the AlCoCrFeNi alloy system, investigations into its wear characteristics at both the nano- and macro-scales are rare, particularly those employing ML approach. Moreover, the relationship among phase evolution, grain size, and wear resistance is still indistinct.

Hence, in this research, a series of CoCrFeNi₂Al_x ($x=0, 0.1, 0.3, 1.0$) HEAs were designed using ML, and the phase and hardness of the alloys were predicted based on the practical considerations and the dataset. The influence of Al content on the microstructure evolution, grain size, and phase components was investigated. Wear resistance at both the nano- and macro-scales was analyzed, and the tribological mechanisms were also discussed.

1 Experiment and Prediction Model Establishment

1.1 Experiment

The CoCrFeNi₂Al_x ($x=0, 0.1, 0.3, 1.0, \text{at}\%$) HEAs were prepared by vacuum-arc-melting method, whose raw materials were Cr, Fe, Ni, Co, and Al metals with purity of 99.99%. To prevent oxidation, the arc-melting process was performed in a high-purity argon atmosphere with Ti-gettering. In the melting

process, electromagnetic stirring method was used to turn the ingot over and remelt the ingot for 6 times to ensure the chemical homogeneity. To obtain the homogeneous microstructure, the as-cast samples were subjected to annealing in a tubular furnace at 1473 K (1200 °C) for 4 h followed by water quenching.

The crystal structure of the alloys was identified by X-ray diffractometer (XRD) using Cu K α radiation at 40 kV and 100 mA, and the 2θ value was in the range of 20°–100° at the scan rate of 2°/min. The microstructure of the samples was examined using transmission electron microscope (TEM). The samples were mechanically ground to approximately 30 μm in thickness and subsequently subjected to electropolishing using the mixed solution of 90vol% alcohol and 10vol% perchloric solution.

The hardness tests were conducted by Vickers hardness tester with load of 500 g and dwell time of 10 s. Each sample was measured multiple times for accurate analysis. The indentation tests were performed at the load of 8000 μN and loading rate of 1000 $\mu\text{N/s}$, and the probe with an effective tip radius of 400 nm was used. The experiments were conducted using the Hysitron Triboscope. Linear reciprocating friction tests of HEAs were conducted using the multifunctional friction and wear tester (NCETRUMT-3MO) at room temperature. A ceramic ball made of Al₂O₃ with diameter of 9.525 mm was selected as the friction counterparts. The test parameters were set as follows: contact load of 10 N, sliding speed of 5 mm/s, and sliding duration of 30 min. Each sample underwent at least three repetitions of the sliding friction test. After the friction test, the wear trace morphologies were observed by scanning electron microscope (SEM) to analyze the wear mechanism. Additionally, energy dispersive spectrometer (EDS) was employed to assess the chemical composition of the wear marks. The wear rate K can be calculated by Eq.(1), as follows:

$$K = \frac{V}{Fd} \quad (1)$$

$$V = \frac{m_0 - m}{\rho} \quad (2)$$

where V is the wear volume, F is the applied load, d is the total sliding distance, m_0 represents the mass before wear, m represents the mass after wear, and ρ represents the density of different alloys measured by the Archimedes drainage method.

For simplification, the CoCrFeNi₂, CoCrFeNi₂Al_{0.1}, CoCrFeNi₂Al_{0.3}, and CoCrFeNi₂Al_{1.0} HEAs are denoted as Al0, Al0.1, Al0.3, and Al1.0, respectively.

1.2 Phase prediction

In this research, data from numerous investigations^[19–24] were used to establish ML-based model for phase prediction, and all necessary data were sourced exclusively from the vacuum arc-melted samples. After data cleaning of the collected alloy data, 656 alloys were obtained, including 306 body-centered cubic (bcc) alloys, 194 face-centered cubic (fcc) alloys, and 156 fcc+bcc alloys. To mitigate the potential impact of imbalanced experiment data on the accuracy of the predictive outcomes, a random oversampling technique was implemented. Among them, the bcc class was the primary

class affected by the imbalance. Following the random oversampling procedure, each class now contained 306 data points (306 bcc, 306 fcc, 306 fcc+bcc).

After the labels for phases were identified, four ML models were established for phase prediction of alloys, namely support vector machine (SVM) model, K-nearest neighbor (KNN) model, neural network (NN) model, and ensemble learning model. In addition, 10-fold cross-validation was employed to minimize the influence of individual samples on the training process. A set of six pertinent features was chosen for phase prediction. These features included enthalpy of mixing (ΔH_{mix}), atomic size difference (δ), valence electron concentration (VEC), entropy/enthalpy ratio (Ω), melting temperature (T_m), and mixing entropy (ΔS_{mix}). The numerical values for these features can be determined by Eq.(3–8)^[25–30], as follows:

$$\Delta H_{\text{mix}} = \sum_{i=1, i \neq j}^n 4c_i c_j \Delta H_{\text{mix}}^{ij} \quad (3)$$

$$\delta = \sqrt{\sum_{i=1}^n c_i \left(1 - \frac{r_i}{\bar{r}}\right)^2} \quad (4)$$

$$\text{VEC} = \sum_{i=1}^n c_i (\text{VEC})_i \quad (5)$$

$$\Delta S_{\text{mix}} = -R \sum_{i=1}^n c_i \ln c_i \quad (6)$$

$$\Omega = \frac{T_m \Delta S_{\text{mix}}}{|\Delta H_{\text{mix}}|} \quad (7)$$

$$T_m = \sum_{i=1}^n c_i T_{m_i} \quad (8)$$

where c_i and c_j are the atomic percentages of the i th and j th components, respectively; $\Delta H_{\text{mix}}^{ij}$ is mixing enthalpy of binary

liquid alloys^[31] using the Miedema method^[32]; r_i is the atomic radius of the i th element; \bar{r} is parameter with $\bar{r} = \sum_{i=1}^n c_i r_i$; VEC_i represents VEC value of the i th element; R is the gas constant of $8.314 \text{ J} \cdot \text{K}^{-1} \cdot \text{mol}^{-1}$; T_{m_i} represents the melting point of the i th element in the alloy.

1.3 Hardness prediction

The hardness datasets of HEAs prepared by vacuum arc-melting were collected from Ref.[33–37]. The eigenvalues are ΔH_{mix} , δ , $\Delta \chi$, VEC, and ΔS_{mix} , and the formula for $\Delta \chi$ is as follows:

$$\Delta \chi = \sqrt{\sum_{i=1}^n c_i (\chi_i - \bar{\chi})^2} \quad (9)$$

$$\bar{\chi} = \sum_{i=1}^n c_i \chi_i$$

where χ_i is the Pauling electronegativity of the i th element.

Based on extensive experiments concerning the number of neurons, a suitable model of back propagation NN optimized by genetic algorithm (GA-BP) was proposed. Typically, NN model consists of three distinct layers—input layer, hidden layer, and output layer, which are interconnected by neurons. The model undergoes iterative training and testing until the error threshold was achieved, resulting in optimal hardness predictions. The element composition and characteristic parameters of CoCrFeNi₂-based alloys were used as inputs.

2 Results and Discussion

2.1 Phase prediction and microstructure characterization

Fig. 1 shows the confusion matrixes for the test data by

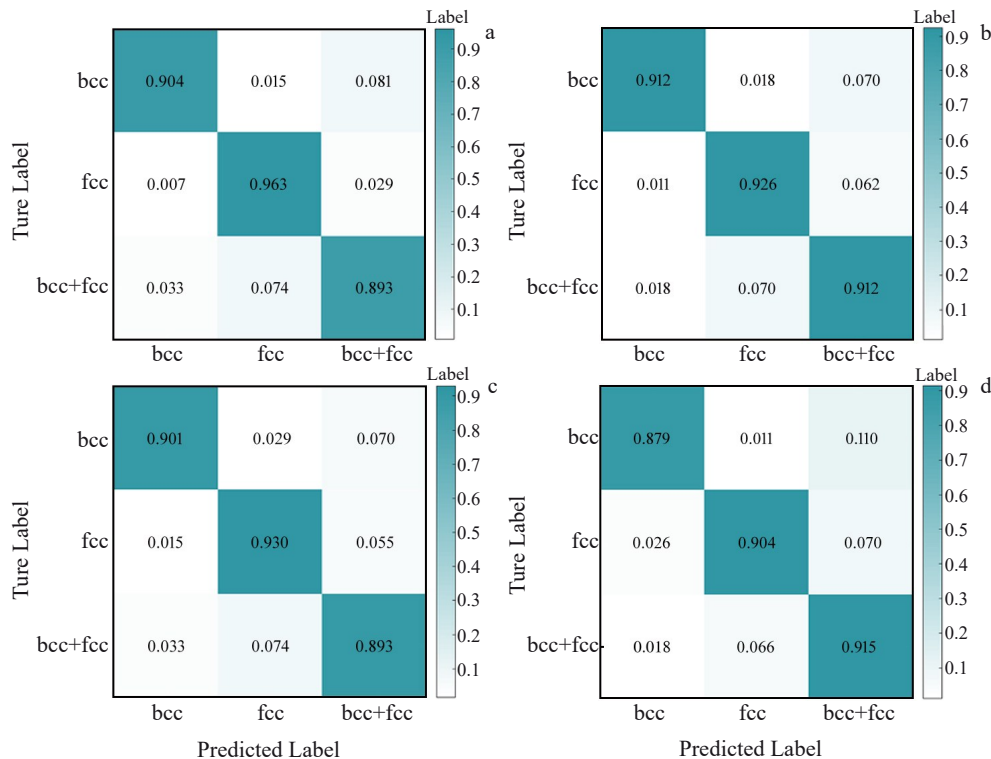


Fig.1 Confusion matrixes of KNN model (a), ensemble learning model (b), NN model (c), and SVM model (d)

different models. Based on the prediction results, it can be observed that KNN model achieves the highest accuracy rate of 96.3% for fcc phase prediction. The accuracy rates of ensemble learning and NN models to predict fcc phase achieve 92.6% and 93.0%, respectively, indicating that these models provide accurate classification for fcc-type alloys. When predicting bcc phase and fcc+bcc phase, KNN model achieves the accuracy rate of 90.4% and 89.3% respectively, and NN model achieves the accuracy rate of 90.1% and 89.3% respectively, indicating similar misclassification rates for KNN and NN models. The ensemble learning model has the highest accuracy rate (91.2%) for the bcc phase prediction, and SVM model has the highest accuracy rate (91.5%) for fcc+bcc phase prediction. Overall, the KNN model can effectively distinguish bcc phase, fcc phase, and mixed (fcc+bcc) phase, and the accuracy rate is approximately 93%.

Receiver operating characteristic (ROC) curves of phase prediction by KNN model are shown in Fig.2, and the above-mentioned prediction results are consistent with the trends in Fig.2, illustrating that the value of area under the curve (AUC) can be primarily used to evaluate the quality of the classification. Generally, the closer the AUC value to 1, the better the performance of the models. AUC values of the models in this research are more than 0.96, which indicates that these models provide accurate predictions for phase identification.

In this research, the KNN-predicted phase components of Al0, Al0.1, Al0.3, and Al1.0 samples are fcc, fcc, fcc, and fcc+

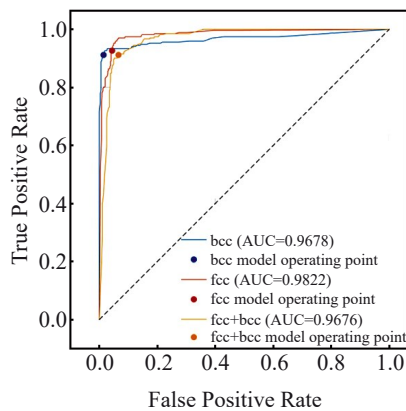


Fig.2 ROC curves of KNN model

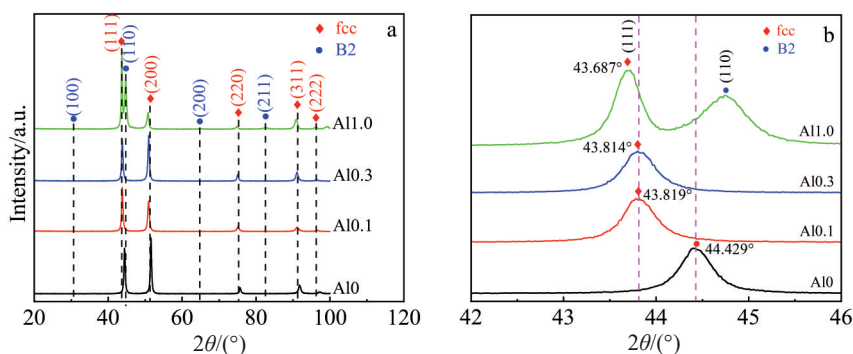


Fig.3 XRD patterns of as-cast $\text{CoCrFeNi}_2\text{Al}_x$ ($x=0, 0.1, 0.3, 1.0$) HEAs: (a) $2\theta=20^\circ\text{--}120^\circ$; (b) $2\theta=42^\circ\text{--}46^\circ$

bcc phases, respectively.

Fig. 3a displays XRD results of $\text{CoCrFeNi}_2\text{Al}_x$ ($x=0, 0.1, 0.3, 1.0$) HEAs. When $x<0.3$, the phase composition of HEAs barely changes, and they all possess the fcc structure. However, with the increase in Al addition ($x=1.0$), HEA is composed of fcc phase plus ordered bcc phase structure (B2 phase). Magnified image of $(111)_{\text{fcc}}$ diffraction peak is displayed in Fig.3b. It can be seen that when x increases from 0 to 1.0, the $(111)_{\text{fcc}}$ diffraction peak shifts to lower 2θ region. Based on XRD results, the lattice constants of the $\text{CoCrFeNi}_2\text{Al}_x$ HEAs with $x=0, 0.1, 0.3$, and 1.0 can be calculated as 0.352 74, 0.357 07, 0.357 62, and 0.358 18 nm, respectively, as listed in Table 1. The theoretical lattice constant equation is expressed in Eq.(10), as follows:

$$a_{\text{mix}} = \sum_{i=1}^n c_i a_i \quad (10)$$

where c_i and a_i are the atomic percentage and lattice constant of the i th component, respectively.

According to Table 1, the theoretical lattice constants of Al0, Al0.1, Al0.3, and Al1.0 samples are 0.327 08, 0.328 48, 0.331 52, and 0.340 09 nm, respectively. It can be seen that the measured values of lattice parameters are consistent with the theoretical ones. According to Bragg's law, the diffraction peak shift can be attributed to the greater radius of Al atom (0.143 nm), which leads to severe lattice distortion.

Because Al0, Al0.1, and Al0.3 samples have similar crystal structures, only the microstructures of Al0.3 sample are used to compare with those of Al1.0 sample for simplification. TEM microstructures of the as-cast $\text{CoCrFeNi}_2\text{Al}_x$ ($x=0.3, 1.0$) HEAs are shown in Fig.4. It can be seen that there is only a simple fcc phase in Al0.3 sample. However, mixed bright and dark stripes can be observed in Al1.0 sample. The spacing of the bright and dark stripes is more than 500 nm but less than 1 μm .

2.2 Wear-related hardness

2.2.1 Training, test, and validation in GA-BP model

79 datasets were split into three subsets for training, test, and validation for GA-BP model building, and the proportion for each subset is 80%, 10%, and 10%, respectively. To ensure the stability of input dataset, the feature scaling function was applied initially to normalize all datasets. The equation for the general formula of characteristic scale is presented

Table 1 Experimental and theoretical lattice constants of CoCrFeNi₂Al_x (x=0, 0.1, 0.3, 1.0) HEAs

Sample	Experimental value/nm	Theoretical value/nm	Error/%
Al0	0.352 74	0.327 08	7.274 5
Al0.1	0.357 07	0.328 48	8.006 8
Al0.3	0.357 62	0.331 52	7.298 2
Al1.0	0.358 18	0.340 09	5.050 5

by Eq.(11)^[38], as follows:

$$x_{\text{scale}} = \frac{x_i - \text{mean}(x_i)}{\text{std}(x_i)} \quad (11)$$

where x_i is the eigenvalue of the i th alloy element.

Using the error trial algorithm, a 10-7-1 backpropagation NN structure was selected for model implementation. During the execution of GA-BP model, the mean square error (MSE) between the desired and predicted values was calculated. The training performance curve is presented in Fig.5. The average error converges to 5.5998×10^{-3} , reaching saturation at the 14th epoch. After several iterations and training sessions, the model achieves satisfactory training results.

2.2.2 Sensitivity analysis

Sensitivity analysis is a technique to investigate how variations in the state or inputs of a model influence the output parameters or environmental conditions. Specifically, it reflects the variation amplitude of model output induced by model parameters. In this research, the input parameters include

alloying elements and characteristic parameters, whereas the output parameters are the hardness values of HEAs. A fully developed model was used in this research, and only one parameter varied at each time with other parameters remaining constant^[39]. The input parameter set with the minimum value is referred as the minimum set, and the input parameter set with the maximum value is termed as the maximum set^[40].

For example, in the sensitivity analysis of Fe, its input parameters vary between maximum and minimum values, whereas other parameters remain constant. Fig.6 shows the sensitivity analyses of different alloying elements by GA-BP hardness prediction model.

The variation trends of minimum and maximum set line segments are basically similar to Fe content variation trend (Fig.6a), which confirms that GA-BP model can effectively predict the influence of Fe content on the hardness of HEAs. Similarly, the outputs for Al and Co content influence exhibit considerable significance. However, the influence of Cr and Ni contents is not as significant as that of other alloying elements. This phenomenon can be primarily attributed to the predictive errors stemming from the limited dataset used during the training, test, and validation.

2.2.3 Comparison between ML prediction and test results

Fig.7a illustrates the correlation coefficients (R) of the GA-BP prediction model. This model can be not only effectively trained ($R=0.994\ 62$) but also verified ($R=0.979\ 39$) with the optimal test set ($R=0.963\ 04$). The final simulation result for

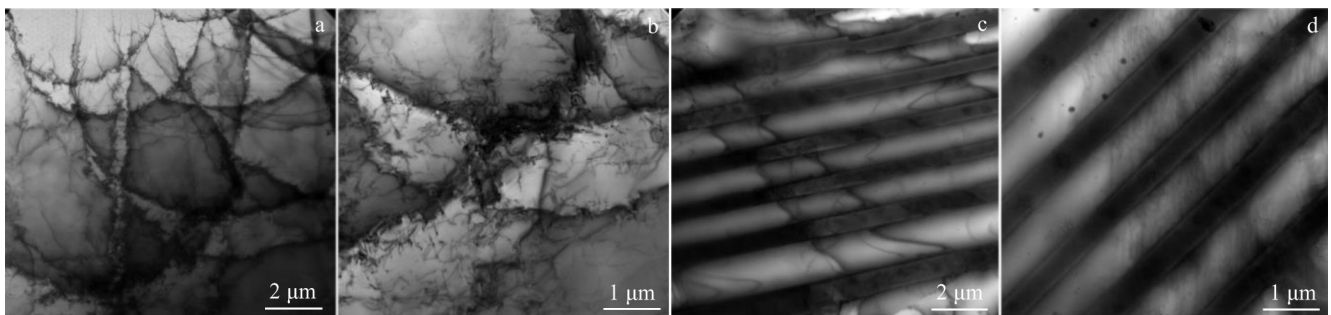


Fig.4 TEM microstructures of as-cast Al0.3 (a–b) and Al1.0 (c–d) samples

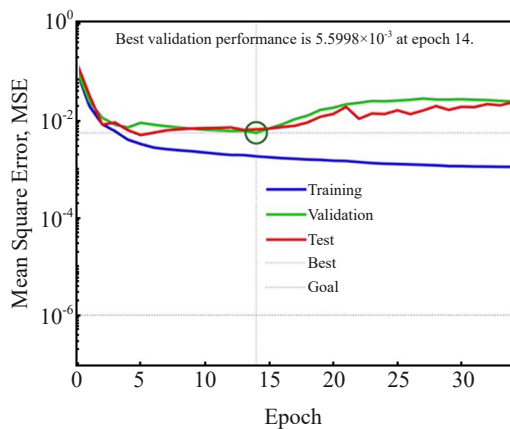


Fig.5 MSE curves during training of GA-BP model for hardness prediction

the entire model is $R=0.980\ 97$, demonstrating that the model predictions are highly consistent with the true values. Fig.7b shows the comparison of hardness obtained by experiment and prediction by GA-BP model. With the increase in Al content, HEA hardness is gradually increased, indicating that Al element can promote the improvement of alloy hardness. The average error of predicted value is 4.6959%, and the average prediction accuracy rate is 95.3041%, as shown in Table 2. The abovementioned results reveal that GA-BP model is highly accurate in hardness prediction of HEAs. Furthermore, compared with that of Al0.1 and Al1.0 samples, the prediction accuracy rate of Al0 and Al0.3 samples is slightly lower, suggesting that the microstructural morphology is a crucial factor influencing the hardness prediction. Briefly, by GA-BP model, the hardness can be well predicted, whose

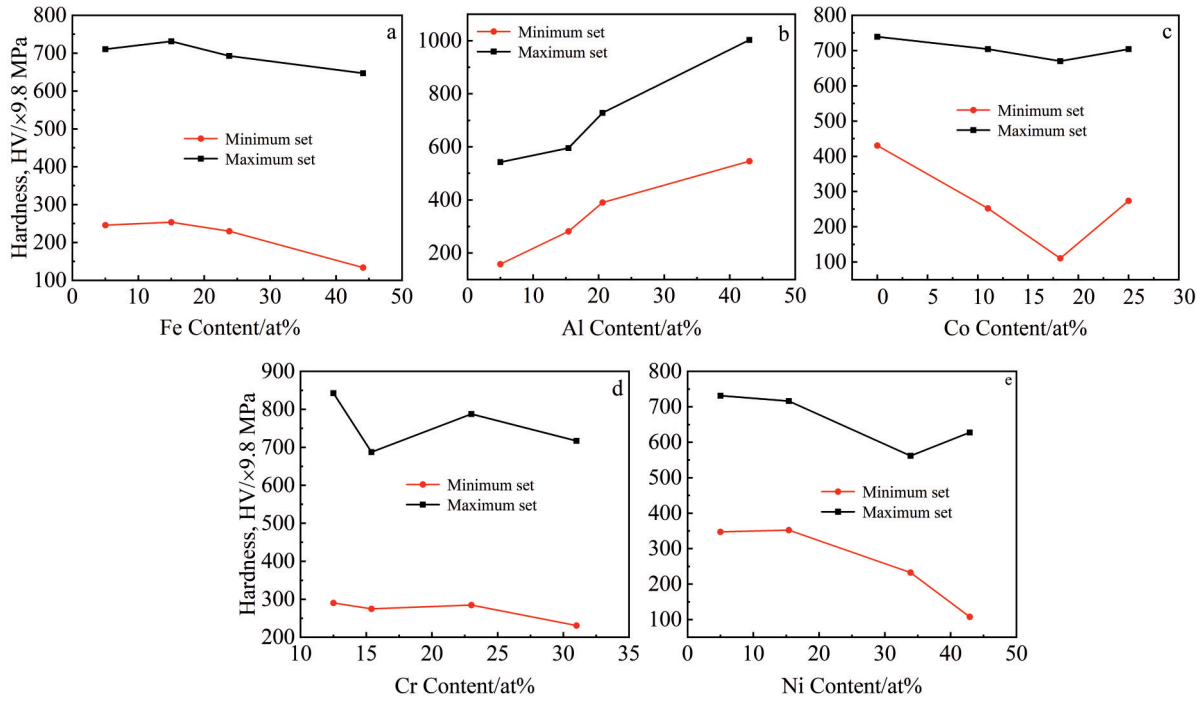


Fig.6 Sensitivity analyses of different alloying elements on CoCrFeNi₂Al_x (x=0, 0.1, 0.3, 1.0) HEAs by GA-BP hardness prediction model: (a) Fe; (b) Al; (c) Co; (d) Cr; (e) Ni

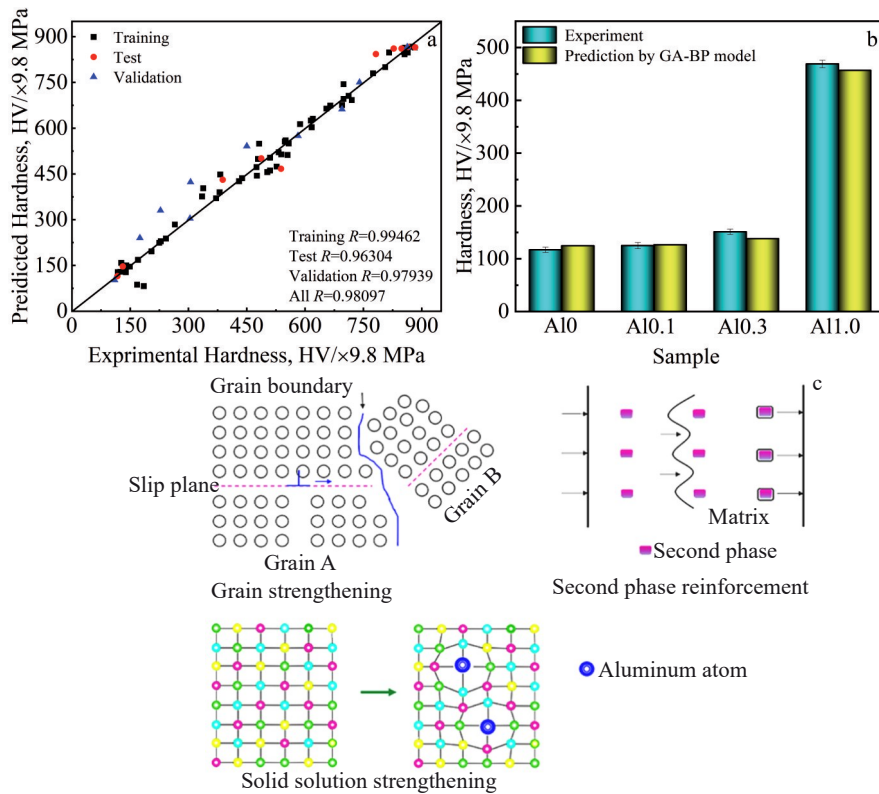


Fig.7 Correlation coefficients of training, test, and validation of GA-BP model (a); comparison of hardness of CoCrFeNi₂Al_x (x=0, 0.1, 0.3, 1.0) HEAs obtained by experiment and prediction by GA-BP model (b); schematic diagram of strengthening modes in CoCrFeNi₂Al_x (x=0, 0.1, 0.3, 1.0) HEAs

correlation and minimum error can achieve 98.7930% and 1.2070%, respectively.

The schematic diagram of strengthening modes in

CoCrFeNi₂Al_x (x=0, 0.1, 0.3, 1.0) HEAs is shown in Fig. 7c. The dislocation exists within the grain slid during plastic deformation. When the dislocations reach the grain boundary,

Table 2 Comparison of hardness of CoCrFeNi₂Al_x (x=0, 0.1, 0.3, 1.0) HEAs obtained by experiment and prediction by GA-BP model

Sample	Experimental hardness/MPa	Predicted hardness/MPa	Error/%	Accuracy/%
Al0	1146.6±49.0	1220.5528	6.4497	93.5503
Al0.1	1225.0±58.8	1239.7862	1.2070	98.7930
Al0.3	1479.8±49.0	1353.3388	8.5458	91.4542
Al1.0	4596.2±68.6	4477.5641	2.5812	97.4188
Average	-	-	4.6959	95.3041

they are obstructed, leading to the blocking and entanglement of the dislocations^[41]. Furthermore, due to the greater radius of Al element, when the Al element is doped into the alloy, the positions of other elements may be occupied. This phenomenon leads to lattice distortion and prevents further dislocation movement. Al0, Al0.1, and Al0.3 samples only have fcc phase, whereas the mixed phase exists in the Al1.0 sample. Due to the existence of the second phase (B2 phase), the movement of dislocations in the fcc phase becomes more and more difficult.

2.3 Nano- and macro-wear resistance

2.3.1 Nano-wear resistance

The typical load (p)-depth (h) curves of the as-cast CoCrFeNi₂Al_x ($x=0, 0.1, 0.3, 1.0$) HEAs are shown in Fig. 8a. The indentation depth is decreased with the increase in Al content. In comparison to HEAs with sole fcc phase, the dual-phase structured HEA exhibits significantly shallower indentation depths. It can be seen that the bcc phase region of Al1.0 sample has the smallest indentation depth, indicating

that it has significantly higher hardness than other samples. The nanohardness (H_N) and elastic modulus (E_m) of CoCrFeNi₂Al_x ($x=0, 0.1, 0.3, 1.0$) HEAs are depicted in Fig. 8b and 8c, respectively. The corresponding H_N and E_m results of bcc and fcc phases of CoCrFeNi₂Al_x ($x=0, 0.1, 0.3, 1.0$) HEAs are shown in Table 3. These results suggest that both the H_N and E_m values are increased with the increase in Al content. Among these HEAs, the bcc phase region of Al1.0 sample exhibits the greatest H_N value (around 5.4 GPa) and E_m value (around 187 GPa). When $x=0$ changes to $x=1.0$, the nanohardness is increased from 3.1 GPa to 5.4 GPa, and the Vickers hardness is increased from 1146.6 MPa to 4596.2 MPa, as listed in Table 2. Furthermore, the elastic modulus results are in agreement with the nanohardness results. Apart from H_N and E_m , the wear resistance can also be evaluated through the nanoindentation test^[42]. The elastic limit of the contact surface is usually reflected by H/E_r value, where H is the hardness and E_r is the reduced elastic modulus, and the plastic deformation resistance of materials under an applied

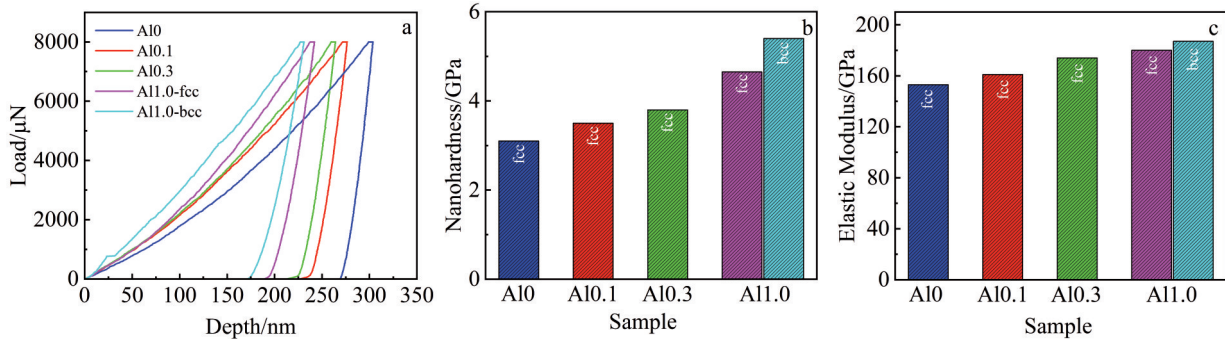


Fig.8 Typical load-depth (p - h) curves of as-cast CoCrFeNi₂Al_x ($x=0, 0.1, 0.3, 1.0$) HEAs (a); nanohardness (b) and elastic modulus (c) of CoCrFeNi₂Al_x ($x=0, 0.1, 0.3, 1.0$) HEAs

load is often reflected by H^3/E_r^2 value^[43]. Therefore, higher H/E_r and H^3/E_r^2 values indicate better wear resistance^[44]. In this research, the E_r value is the Young's modulus, as follows:

$$\frac{1}{E_r} = \frac{1 - \nu_i^2}{E_i} + \frac{1 - \nu_s^2}{E_s} \quad (12)$$

where $E_i=1141$ GPa and $\nu_i=0.07$ are the Young's modulus and Poisson's ratio of the indenter, respectively; E_s and $\nu_s=0.26$ ^[45] are the Young's modulus and Poisson's ratio of HEA sample, respectively.

The H and E_r values of CoCrFeNi₂Al_x ($x=0, 0.1, 0.3, 1.0$) HEAs are shown in Table 4. The results demonstrate that with

Table 3 Nanohardness (H_N) and elastic modulus (E_m) of different phases in CoCrFeNi₂Al_x ($x=0, 0.1, 0.3, 1.0$) HEAs

Sample	Phase	Nanohardness, H_N /GPa	Elastic modulus, E_m /GPa
Al0	fcc	3.1	153
Al0.1	fcc	3.5	161
Al0.3	fcc	3.8	174
Al1.0	fcc	4.7	180
	bcc	5.4	187

the increase in Al content, both H and E_r show an increasing trend. However, the H increment is larger than E_r increment. As shown in Table 4, both H/E_r and H^3/E_r^2 values show increasing trend, which indicates that the wear resistance of $\text{CoCrFeNi}_2\text{Al}_x$ ($x=0, 0.1, 0.3, 1.0$) HEAs is increased with the increase in Al content.

2.3.2 Macro-wear resistance

The tribological characteristics of $\text{CoCrFeNi}_2\text{Al}_x$ ($x=0, 0.1, 0.3, 1.0$) HEAs under linear reciprocating motion mode were investigated. Fig. 9 presents the wear test results of the $\text{CoCrFeNi}_2\text{Al}_x$ ($x=0, 0.1, 0.3, 1.0$) HEAs. Fig. 9a illustrates the fluctuation curves of COF of different samples over 1800 s. COF of A10 sample is 0.8140 and that of A11.0 sample is 0.4891, inferring that A11.0 sample has the optimal wear resistance. Nevertheless, when $x=0.3$, COF increases to 0.9976. The Al addition leads to a notable enhancement in wear resistance with the wear rate decreasing from $3.591 \times 10^{-4} \text{ mm}^3 \cdot \text{N}^{-1} \cdot \text{m}^{-1}$ to $2.332 \times 10^{-4} \text{ mm}^3 \cdot \text{N}^{-1} \cdot \text{m}^{-1}$, as shown in Fig. 9b. The improvement in wear resistance of the $\text{CoCrFeNi}_2\text{Al}_x$ HEAs can be attributed to the optimized phase composition and particle size. Generally, the wear resistance has a positive correlation with the hardness^[46]. The fcc phase can be regarded as a comparatively soft phase. Hence, the CoCrFeNi_2 HEA, which only consists of fcc phase, shows the worst wear resistance. Doping Al results in the formation of eutectic

Table 4 H/E_r and H^3/E_r^2 values of $\text{CoCrFeNi}_2\text{Al}_x$ ($x=0, 0.1, 0.3, 1.0$) HEAs

Sample	H/GPa	E_r/GPa	H/E_r	H^3/E_r^2
A10	3.1	143.549 32	0.021 60	0.001 50
A10.1	3.5	150.072 77	0.023 32	0.001 90
A10.3	3.8	160.494 32	0.023 68	0.002 13
A11.0	5.0	167.965 61	0.029 92	0.004 50

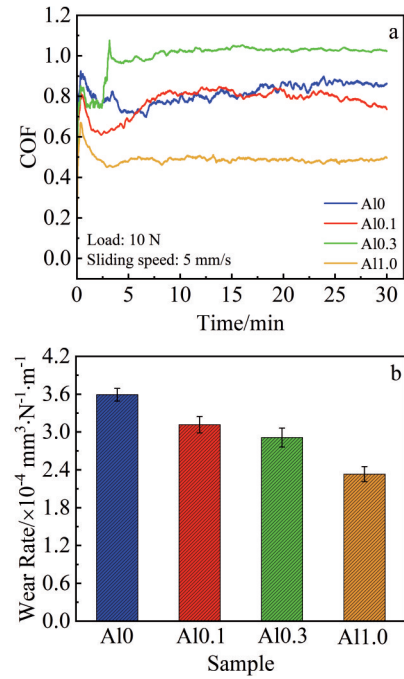


Fig.9 COF curves (a) and wear rates (b) of $\text{CoCrFeNi}_2\text{Al}_x$ ($x=0, 0.1, 0.3, 1.0$) HEAs

structure consisting of both fcc and B2 phases. Therefore, the significant improvement in wear resistance of A11.0 sample can be attributed to the presence of high-hardness B2 phase. This result is in agreement with the high H/E_r and H^3/E_r^2 values of A11.0 sample. Moreover, COF values exhibit a sharp increase at the beginning of friction and then stabilize. COF of A10 sample gradually stabilizes after approximately 5 min. After Al addition, the run-in time is prolonged to 10 min. The increased hardness poses greater resistance against plastic deformation, prolonging the duration for the establishment of

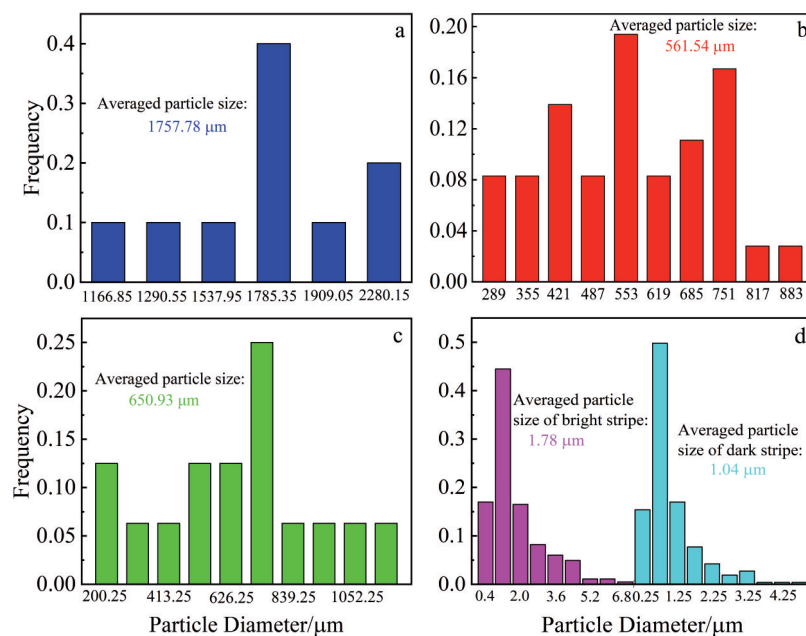


Fig.10 Particle size distributions of A10 (a), A10.1 (b), A10.3 (c), and A11.0 (d) samples

stable friction layer.

It is worth noting that COF of the Al0.3 sample is quite different from that of the Al0.1 sample, which may be attributed to the grain size. According to XRD results, the trace addition of Al does not induce the phase transformation. Thus, the Al0.3 sample displays the simple fcc structure just as the Al0.1 and Al0 samples. However, the average grain size of the Al0.1 sample is much greater than that of the Al0.3 sample. The particle size distributions of CoCrFeNi₂Al_x (x=0, 0.1, 0.3, 1.0) HEAs are shown in Fig.10. It is reported that the grain size has close relationship with the hardness, which can be explained by the Hall-Petch equation^[47-50], as follows:

$$H = H_0 + K_y d^{-\frac{1}{2}} \quad (13)$$

where $H_0 \approx 558.40 \text{ MPa}^{[50]}$, $K_y = 112.51^{[50]}$, and d is the particle

size.

The wear surfaces of CoCrFeNi₂Al_x (x=0, 0.1, 0.3, 1.0) HEAs are shown in Fig.11. It can be seen that the Al0 sample exhibits notably more pronounced spalling phenomenon, indicating severe plastic deformation. This phenomenon is primarily due to the low hardness and high plasticity of fcc phase coupled with the shear forces engendered during the friction experiments. Therefore, Al0 sample is particularly susceptible to plastic deformation and extensive spalling can also be observed under the sliding of friction pair. The surface of the Al0 sample has numerous parallel grooves along the sliding direction, resulting from the severe abrasive wear during friction. Similar wear characteristics can also be observed on the Al0.1 sample surface (Fig. 11b). Therefore, the wear mechanisms of the Al0 and Al0.1 samples involve

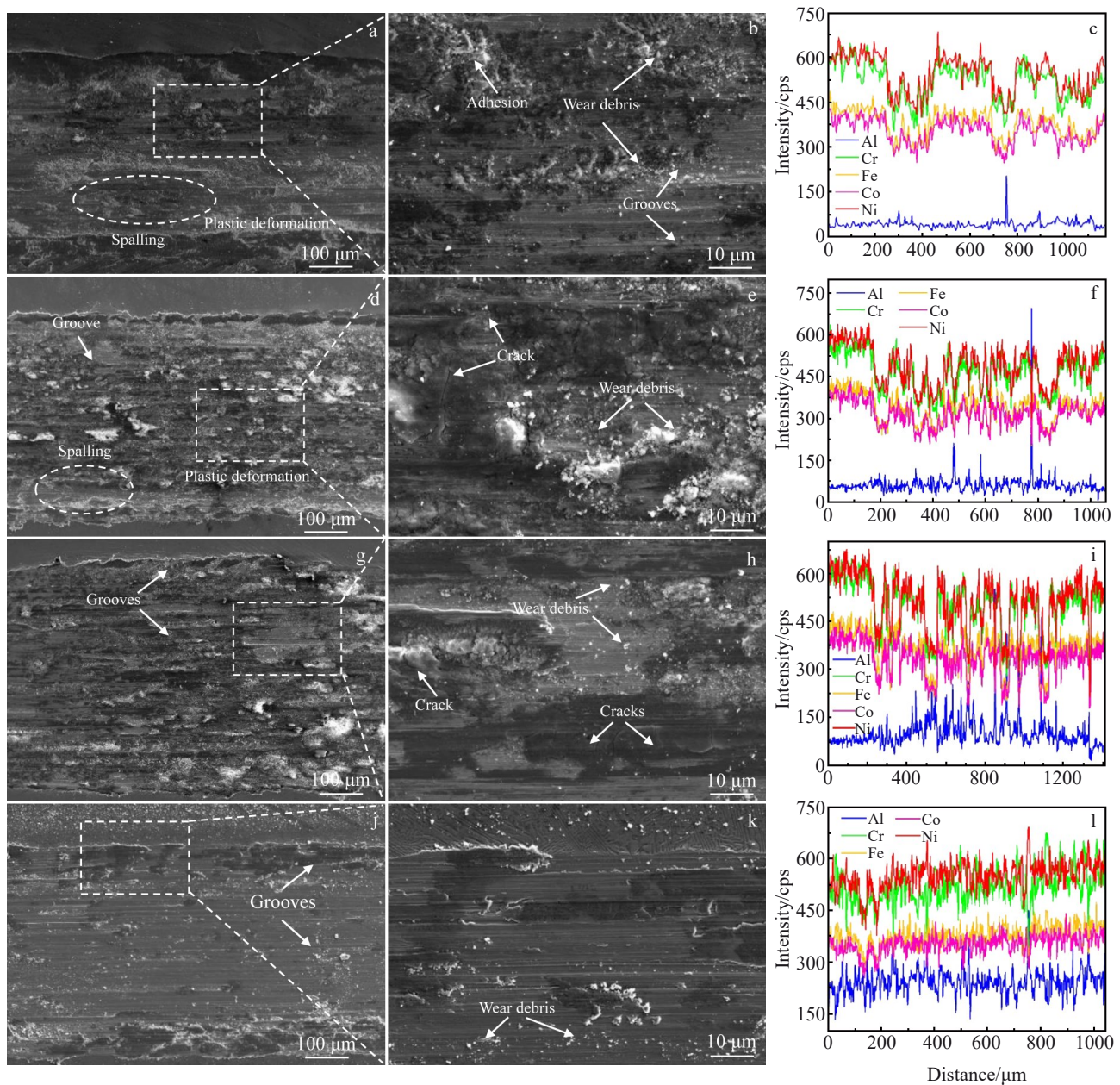


Fig.11 SEM wear morphologies (a-b, d-e, g-h, j-k) and EDS element distributions (c, f, i, l) of Al0 (a-c), Al0.1 (d-f), Al0.3 (g-i), and Al1.0 (j-l) samples after friction wear tests at room temperature

severe adhesive and abrasive wear. Under sharp contrast condition, the wear surfaces of the Al0.3 sample exhibit microcrack damages (Fig. 11c), which can be attributed to fatigue crack propagation caused by stress concentration. This is attributed to the inferior crack resistance of CoCrFeNi₂-based HEA, which leads to the occurrence of cracks under high load wear conditions, consequently reducing the service life^[51]. The presence of cracks increases the roughness of the contact surface, leading to brittle spalling and the increase in wear rate. Therefore, at room temperature, the mechanical properties greatly influence the wear resistance. The wear marks of abrasive traces along with a few grooves can be observed, indicating that the wear mechanism of the Al0.3 sample involves both abrasive wear and fatigue wear^[52]. The surface wear marks of the Al1.0 sample are uniform without apparent adhesion or cracking (Fig. 11d). Some abrasion debris and furrows can be observed, indicating that the predominant form of wear is mild plastic deformation and abrasive wear.

Based on the wear morphologies and EDS results, it can be inferred that increasing the Al content can enhance the surface hardness of HEA. The change in composition leads to a transition in the wear mechanism from severe adhesive wear to abrasive wear. Consequently, the wear resistance of HEA is significantly enhanced.

3 Conclusions

1) With the increase in Al content, the crystalline structure of CoCrFeNi₂Al_x ($x=0, 0.1, 0.3, 1.0$) HEAs varies from fcc phase to mixed fcc+bcc phase.

2) Among the phase prediction models (SVM, KNN, NN, and ensemble learning), KNN model possesses the highest accuracy rate of approximately 93%. By GA-BP model, the hardness can be well predicted, whose correlation and minimum error can achieve 98.7930% and 1.2070%, respectively.

3) With the increase in Al content from $x=0$ to $x=1.0$, the nanohardness is increased from 3.1 GPa to 5.4 GPa, and the Vickers hardness is increased from 1146.6 MPa to 4596.2 MPa.

4) The wear rate decreases from $3.591 \times 10^{-4} \text{ mm}^3 \cdot \text{N}^{-1} \cdot \text{m}^{-1}$ to $2.332 \times 10^{-4} \text{ mm}^3 \cdot \text{N}^{-1} \cdot \text{m}^{-1}$ with the increase in Al addition. For Al0 and Al0.1 samples, severe adhesive wear and abrasive wear occur during wear tests. For Al0.3 sample, the abrasive wear and fatigue wear are dominated wear mechanisms. For Al1.0 sample, only mild plastic deformation and abrasive wear occur.

References

- 1 Yeh Jien Wei, Chen Swe Kai, Lin Su Jien et al. *Advanced Engineering Materials*[J], 2004, 6(5): 299
- 2 Zhang Yong, Zuo Tingting, Tang Zhi et al. *Progress in Materials Science*[J], 2014, 61: 1
- 3 Feng Li, Wang Mengqi, Zhao Yanchun et al. *Rare Metal Materials and Engineering*[J], 2024, 53(1): 85 (in Chinese)
- 4 Yuan Kunquan. *Rare Metal Materials and Engineering*[J], 2023, 52(11): 3981 (in Chinese)
- 5 Yoav Lederer, Cormac Toher, Kenneth Vecchio et al. *Acta Materialia*[J], 2018, 159: 364
- 6 Senkov O, Miller J, Miracle D B et al. *Nature Communications*[J], 2015, 6(3): 6529
- 7 Zhang F, Zhang C, Chen S L et al. *Calphad*[J], 2014, 45: 1
- 8 Bobbili R, Ramakrishna B. *Materials Today Communications*[J], 2023, 36: 106674
- 9 Guo Qingwei, Xu Xiaotao, Pei Xiaolong et al. *Journal of Materials Research and Technology*[J], 2023, 22: 3331
- 10 Li Shuai, Li Shu, Liu Dongrong et al. *Computational Materials Science*[J], 2022, 205: 111185
- 11 Oñate Angelo, Sanhueza Juanpablo, Zegpi Diabb et al. *Journal of Alloys and Compounds*[J], 2023, 962: 171224
- 12 Jiang Junjie, Zhang Aijun, Han Jiasheng et al. *Tribology International*[J], 2024, 191: 109154
- 13 Yu Yuan, He Feng, Qiao Zhuhui et al. *Journal of Alloys and Compounds*[J], 2019, 775: 1376
- 14 Zhang Ruiyang, Tulugan Kelimu, Zhang Aijun et al. *Journal of Materials Engineering and Performance*[J], 2022, 31: 984
- 15 Archard J F, Hirst W. *Proceedings of the Royal Society A*[J], 1956, 236(1206): 397
- 16 Liu Hao, Gao Qiang, Dai Jianbo et al. *Tribology International*[J], 2022, 172: 107574
- 17 Xing Xuwei, Liu Ying, Hu Jinkang et al. *Materials Research Express*[J], 2022, 9: 036510
- 18 Wu Mingyu, Chen Ke, Xu Zhen et al. *Wear*[J], 2020, 462–463: 203493
- 19 Miracle D B, Senkov O N. *Acta Materialia*[J], 2017, 122: 448
- 20 Ye Y F, Wang Q, Lu J et al. *Materials Today*[J], 2016, 19: 349
- 21 Couzinié J P, Senkov O N, Miracle D B et al. *Data in Brief*[J], 2018, 21: 1622
- 22 Gorsse S, Nguyen M H, Senkov O N et al. *Data in Brief*[J], 2018, 21: 2664
- 23 Yang X, Zhang Y. *Materials Chemistry and Physics*[J], 2012, 132(2–3): 233
- 24 Chang H N, Tao Y W, Liaw P K et al. *Journal of Alloys and Compounds*[J], 2022, 921: 166149
- 25 Guo Sheng, Ng Chun, Lu Jian et al. *Journal of Applied Physics*[J], 2011, 109: 103505
- 26 Zhu Wenhan, Huo Wenyi, Wang Shiqi. *Journal of Materials Research and Technology*[J], 2022, 18: 800
- 27 Jeong Il Seok, Lee Joo Hyoung. *Materials & Design*[J], 2023, 227: 111709
- 28 Zhao Fengyuan, Ye Yicong, Zhang Zhouan et al. *Rare Metal Materials and Engineering*[J], 2023, 52(4): 1192
- 29 Poletti M G, Battezzati L. *Acta Materialia*[J], 2014, 75: 297
- 30 Xue Yuan, Shan Guibin, Pan Ruilin et al. *Rare Metal Materials and Engineering*[J], 2024, 53(1): 56 (in Chinese)
- 31 Takeuchi A, Inoue A. *Materials Transactions*[J], 2005, 46(12):

- 2817
- 32 De Boer F R, Mattens W, Boom R et al. *Cohesion in Metals: Transition Metal Alloys*[M]. Amsterdam: North-Holland, 1988
- 33 Zhang Yifan, Ren Wei, Wang Weili et al. *Journal of Alloys and Compounds*[J], 2023, 945: 169329
- 34 Chen Cun, Ma Leiying, Zhang Yong et al. *Intermetallics*[J], 2023, 154: 107819
- 35 Wu Shaoyu, Xu Xiaoqian, Yang Shani et al. *Ceramics International*[J], 2023, 49: 21561
- 36 Ye Yicong, Li Yahao, Ouyang Runlong et al. *Computational Materials Science*[J], 2023, 223: 112140
- 37 Sheetal Kumar Dewangan, Ashutosh Sharma, Hansung Lee et al. *Journal of Alloys and Compounds*[J], 2023, 958: 170359
- 38 Aksoy S, Haralick R M. *Pattern Recognition Letters*[J], 2001, 22: 563
- 39 Sandeep Chaudhary, Umesh Pendharkar, Ashok Nagpal. *Steel and Composite Structures*[J], 2007, 7(3): 219
- 40 Pendharkar U, Chaudhary S, Nagpal A K. *Structural Engineering and Mechanics*[J], 2010, 36(2): 165
- 41 Wang Enhao, Li Jiaqi, Kang Fuwei et al. *Journal of Materials Research and Technology*[J], 2024, 28: 967
- 42 Fornell J, Steenberge N V, Varea A et al. *Journal of the Mechanical Behavior of Biomedical Materials*[J], 2011, 4(8): 1709
- 43 Chen Hao, Cui Hongzhi, Jiang Di et al. *Journal of Alloys and Compounds*[J], 2022, 899: 163277
- 44 Ehtemam Haghighi Shima, Cao Guanghui, Zhang Laichang. *Journal of Alloys and Compounds*[J], 2017, 692: 892
- 45 Ye Y X, Lu Z P, Nieh T G. *Scripta Materialia*[J], 2017, 130: 64
- 46 Zhao Yanchun, Song Haizhuan, Ma Huwen et al. *Rare Metal Materials and Engineering*[J], 2024, 53(1): 102 (in Chinese)
- 47 Hidesato Mabuchi, Toshiei Hasegawa, Tadashi Ishikawa. *ISIJ International*[J], 1999, 39: 477
- 48 Hurley P J, Muddle B C, Hodgson P D. *Metallurgical and Materials Transactions A*[J], 2001, 6(32): 1507
- 49 Hidaka H, Tsuchiyama T, Takaki S. *Scripta Materialia*[J], 2001, 44(8-9): 1503
- 50 Kunal B, Keche A J, Gogte C L et al. *Materials Today: Proceedings*[J], 2020, 26(Part 2): 3173
- 51 Kenneth Holmberg, Anssi Laukkanen, Helena Ronkainen et al. *Tribology International*[J], 2009, 42(1): 137
- 52 Jing Yongzhi, Fang Yongchao, Cui Xiufang et al. *Tribology International*[J], 2023, 185: 108551

Al含量对CoCrFeNi₂基高熵合金的微观结构及摩擦性能的影响

张梦迪, 张改梅, 罗崇玮, 徐汉清

(河北大学 质量技术监督学院, 河北 保定 071002)

摘要: 使用了4种机器学习算法来预测高熵合金(HEA)的固溶体相。为了提高模型的准确率,采用了K折交叉验证。结果表明,K近邻(KNN)算法可以有效地区分体心立方(bcc)相、面心立方(fcc)相和混合(fcc+bcc)相,准确率为93%。随后,制备了CoCrFeNi₂Al_x(x=0、0.1、0.3和1.0) HEA,并采用X射线衍射仪和能量色散光谱仪对其进行了表征,其相由单一的fcc相转变为fcc+bcc相,这与机器学习相预测的结果一致。此外,还评估了Al含量对CoCrFeNi₂Al_x(x=0、0.1、0.3和1.0) HEAs的微观结构及摩擦性能的影响。结果表明,随着Al含量的增加,纳米硬度和显微硬度分别增加了约45%和75%。弹性极限参数 H/E_c 从0.0216增加到0.030,而抗塑性形变参数 H^3/E_c^2 从0.0014增加到0.0045,这表明随着Al含量的增加,纳米硬度得到了改善。此外,随着Al含量的增加,磨损率降低了35%。本研究为设计节能和省时的HEA制备方法提供了新思路。

关键词: 机器学习; 高熵合金; 硬度; 耐磨性能

作者简介: 张梦迪,女,1988年生,博士,教授,河北大学质量技术监督学院,河北 保定 071002, E-mail: mengdizhang@hbu.edu.cn